PHOTONICS Research

Local characterization of the polarization state of 3D electromagnetic fields: an alternative approach

Rosario Martínez-Herrero,[1] David Maluenda,[2] Marcos Aviñoá,[2] Artur Carnicer,[2] Ignasi Juvells,[2] and Ángel S. Sanz[1,*]

[1]Departamento de Óptica, Universidad Complutense de Madrid (UCM), Ciudad Universitaria, 28040 Madrid, Spain
[2]Facultat de Física, Departament de Física aplicada, Universitat de Barcelona (UB), Martí i Franquès 1, 08028 Barcelona, Spain
*Corresponding author: a.s.sanz@fis.ucm.es

Received 27 February 2023; revised 17 May 2023; accepted 17 May 2023; posted 23 May 2023 (Doc. ID 488703); published 28 June 2023

A precise knowledge of the polarization state of light is crucial in technologies that involve the generation and application of structured light fields. The implementation of efficient methods to determine and characterize polarization states is mandatory; more importantly, these structured light fields must be at any spatial location at a low expense. Here, we introduce a new characterization method that relies on a rather convenient description of electric fields without neglecting their 3D nature. This method is particularly suitable for highly focused fields, which exhibit important polarization contributions along their propagation direction in the neighborhood of the focal region; i.e., the contributions out of the planes transverse to the optical axis, conventionally used to specify the polarization state of these fields. As shown, the method allows the extraction of information about the three field components at relatively low computational and experimental costs. Furthermore, it also allows characterization of the polarization state of a field in a rather simple manner. To check the feasibility and reliability of the method, we determined both analytically and experimentally the local polarization states for a series of benchmark input fields with it, finding excellent agreement between the theory and experiment.

https://doi.org/10.1364/PRJ.488703

1. INTRODUCTION

The generation of structured light has acquired a pivotal role in different technological fields. These fields cover areas as diverse as the design and application of nanostructures, ultrahigh-resolution optical microscopy, ultradense information storage and transfer, high-harmonic generation (HHG), and terahertz (THz) radiation generation, just to cite a few remarkable examples. Hence, methods to determine and characterize the properties of structured light [both its dynamic field parameters (e.g., energy flux, momentum, and angular momentum) and its polarization features] are also receiving much attention [1–5].

Highly focused fields with a nonhomogeneous polarization state distribution constitute a particular instance within this scenario because of their potential applications in fields such as microscopy, nonlinear optics, and plasmonics [5–37]. In these circumstances, the (input) vector field at the entrance pupil of the focusing system must be tailored to the specific requirements involved in the problem or experiment considered. A combination of diffractive, interferometric, and holographic techniques is often used to achieve full control over the complex amplitude and polarization distributions of the input field.

That scenario leads us to a nontrivial question: how can we specify the polarization state in the focal region of imaging systems with a high numerical aperture (NA), where the 3D nature of the electromagnetic field cannot be neglected? In two dimensions, for instance, choosing the z axis as the reference or privileged direction allows the specification of the polarization state by simply inspecting the time behavior exhibited by the field transverse components. This procedure works very well for plane waves and for locally nearly flat and parallel wavefronts. However, what about more general 3D scenarios, where the wavefronts might undergo important space variations from point to point, as it happens with highly focused fields? In other words, how can we characterize the polarization state of a general 3D field if the current understanding of polarization lies on a 2D representation?

An answer to that question has been proposed in the literature in terms of a generalization of the Stokes parameters [38–40], based on the so-called Gell-Mann matrices, borrowed from the field of particle physics. These eight 3×3 traceless, Hermitian matrices span the usual Lie algebra because they can generate elements of the SU(3) symmetry group, in analogy to the three 2×2 traceless Pauli matrices that generate the

SU(2) symmetry group. In this work, though, instead of directly dealing with the complexity inherent to the full 3D problem, we introduce an alternative method that enables efficient theoretical and experimental analysis, but without abandoning the conceptual appeal involved in the usual formulation of 2D Stokes parameters.

More specifically, our method relies on the known idea that the field can be recast in terms of its real and imaginary vector components [41]. By means of a convenient local rotation of these components, we can determine the direction vectors that specify the orthogonal directions in the Argand–Gauss plane that contains the field components at a specific point. In the case of highly focused paraxial fields, this means that at any given position along the optical z axis (where the 2D transverse Stokes parameters are computed), there is a family of planes, each one characterized by its own local normal direction vector. This direction is used to describe locally the polarization state without requiring more sophisticated calculations; for instance, the calculations mentioned above based on Gell-Mann matrices. We know that the usual transverse Stokes parameters S_α ($\alpha = 0, 1, 2, 3$) only provide (or are obtained from) information from the transverse field components, which implies neglecting the 3D nature of the field. In sharp contrast, the method proposed here allows a full 3D characterization of the polarization state. To this end, the method relies on information supplied by both a new class of local Stokes parameters (henceforth denoted as $\tilde{S}_\alpha$) and the (also locally computed) direction vector normal to the plane that contains the vibrating field.

To illustrate the feasibility and reliability of the methodology, 3D highly focused fields generated by spatially localized fields with a Gaussian envelop and different polarization states are considered. The three components for these fields are determined analytically at the focal plane by means of the Richards–Wolf integral [42] and measured experimentally by making use of the procedure in Ref. [43]. In both theory and experiment, the local plane containing the vector field is determined from the field components, which allows the value for the local Stokes parameters around the focal region to be inferred. As shown, there is an excellent agreement between the theory and the experiment when the results obtained from the numerical simulations and the experimental data are compared. Although the present analysis concerns the focal area, it should be stressed that it can readily be extended to any other region or plane along the system's optical axis since the method itself is not limited to the focal region.

2. THEORY

Consider an arbitrary quasi-monochromatic vector field $\mathbf{E}(\mathbf{r})$ with three nonvanishing components. Since focusing (and propagation, in general) takes place mainly along the z direction, this field can be recast as

$$\mathbf{E}(\mathbf{r}_\perp, z) = \mathbf{E}_r(\mathbf{r}_\perp, z) + i\mathbf{E}_i(\mathbf{r}_\perp, z), \tag{1}$$

where $\mathbf{r}_\perp = (x, y)$ is the transverse position vector, and $\mathbf{E}_r(\mathbf{r}_\perp, z)$ and $\mathbf{E}_i(\mathbf{r}_\perp, z)$ are both real vector fields in a 3D space. These two vector fields can, in turn, be rewritten at any spatial point $(\mathbf{r}_\perp, z)$ in terms of a local, orthogonal vector basis set. A first suitable choice to determine this basis set consists in directly applying the well-known Gram–Schmidt orthogonalization procedure. Here, we considered an alternative and more convenient choice, consisting of constructing a basis set formed by two orthogonal vectors contained within the same plane that also contains $\mathbf{E}_r$ and $\mathbf{E}_i$, and the normal vector that defines this plane (the third component of the basis set).

Specifically, this is accomplished first by means of a local rotation at $(\mathbf{r}_\perp, z)$ [41]:

$$\mathbf{P}(\mathbf{r}_\perp, z) = \cos\,\alpha(\mathbf{r}_\perp, z)\mathbf{E}_r(\mathbf{r}_\perp, z) + \sin\,\alpha(\mathbf{r}_\perp, z)\mathbf{E}_i(\mathbf{r}_\perp, z), \tag{2a}$$

$$\mathbf{Q}(\mathbf{r}_\perp, z) = -\sin\,\alpha(\mathbf{r}_\perp, z)\mathbf{E}_r(\mathbf{r}_\perp, z) + \cos\,\alpha(\mathbf{r}_\perp, z)\mathbf{E}_i(\mathbf{r}_\perp, z), \tag{2b}$$

where the spatially dependent local rotation angle $\alpha(\mathbf{r}_\perp, z)$ is

$$\tan\,2\alpha(\mathbf{r}_\perp, z) = \frac{2\mathbf{E}_r(\mathbf{r}_\perp, z)\cdot\mathbf{E}_i(\mathbf{r}_\perp, z)}{\|\mathbf{E}_r(\mathbf{r}_\perp, z)\|^2 - \|\mathbf{E}_i(\mathbf{r}_\perp, z)\|^2}. \tag{3}$$

This angle arises from the orthogonality condition $\mathbf{P}(\mathbf{r}_\perp, z)\cdot\mathbf{Q}(\mathbf{r}_\perp, z) = 0$. Once $\mathbf{P}(\mathbf{r}_\perp, z)$ and $\mathbf{Q}(\mathbf{r}_\perp, z)$ are known, the normal to the plane containing these two new vector fields is then readily obtained as

$$\mathbf{N}(\mathbf{r}_\perp, z) = \mathbf{P}(\mathbf{r}_\perp, z)\times\mathbf{Q}(\mathbf{r}_\perp, z). \tag{4}$$

Physically, this normal vector coincides with the electric contribution to the spin angular momentum density [1]. In terms of the new basis set, the vector field $\mathbf{E}(\mathbf{r}_\perp, z)$ reads as

$$\mathbf{E}(\mathbf{r}_\perp, z) = [\mathbf{P}(\mathbf{r}_\perp, z) + i\mathbf{Q}(\mathbf{r}_\perp, z)]e^{i\alpha(\mathbf{r}_\perp, z)}, \tag{5}$$

with its polarization plane being perpendicular to $\mathbf{N}(\mathbf{r}_\perp, z)$. Note that this also holds if we directly consider the real and imaginary components of the field by virtue of the invariance property

$$\mathbf{E}_r(\mathbf{r}_\perp, z)\times\mathbf{E}_i(\mathbf{r}_\perp, z) = \mathbf{P}(\mathbf{r}_\perp, z)\times\mathbf{Q}(\mathbf{r}_\perp, z) = \mathbf{N}(\mathbf{r}_\perp, z). \tag{6}$$

The contribution of the new basis vectors to the 3D field $\mathbf{E}(\mathbf{r}_\perp, z)$ is

$$E_P(\mathbf{r}_\perp, z) = \frac{\mathbf{P}(\mathbf{r}_\perp, z)}{\|\mathbf{P}(\mathbf{r}_\perp, z)\|}\cdot\mathbf{E}(\mathbf{r}_\perp, z) = \|\mathbf{P}(\mathbf{r}_\perp, z)\|e^{i\alpha(\mathbf{r}_\perp, z)}, \tag{7a}$$

$$E_Q(\mathbf{r}_\perp, z) = \frac{\mathbf{Q}(\mathbf{r}_\perp, z)}{\|\mathbf{Q}(\mathbf{r}_\perp, z)\|}\cdot\mathbf{E}(\mathbf{r}_\perp, z) = i\|\mathbf{Q}(\mathbf{r}_\perp, z)\|e^{i\alpha(\mathbf{r}_\perp, z)}, \tag{7b}$$

$$E_N(\mathbf{r}_\perp, z) = \frac{\mathbf{N}(\mathbf{r}_\perp, z)}{\|\mathbf{N}(\mathbf{r}_\perp, z)\|}\cdot\mathbf{E}(\mathbf{r}_\perp, z) = 0. \tag{7c}$$

These expressions show that the field is, in general, elliptically polarized within the plane normal to $\mathbf{N}(\mathbf{r}_\perp, z)$.

Because the field is contained within a plane determined locally by the normal $\mathbf{N}(\mathbf{r}_\perp, z)$, we introduce a set of local Stokes parameters, defined in a similar way to the usual transverse Stokes parameters; that is, if the latter are given as

$$S_0(\mathbf{r}_\perp, z) = |E_x(\mathbf{r}_\perp, z)|^2 + |E_y(\mathbf{r}_\perp, z)|^2, \tag{8a}$$

$$S_1(\mathbf{r}_\perp, z) = |E_x(\mathbf{r}_\perp, z)|^2 - |E_y(\mathbf{r}_\perp, z)|^2, \tag{8b}$$

$$S_2(\mathbf{r}_\perp, z) = 2\,\mathrm{Re}[E_x^*(\mathbf{r}_\perp, z)E_y(\mathbf{r}_\perp, z)], \tag{8c}$$

$$S_3(\mathbf{r}_\perp, z) = 2\,\mathrm{Im}[E_x^*(\mathbf{r}_\perp, z)E_y(\mathbf{r}_\perp, z)], \tag{8d}$$

in terms of the transverse components of the field $\mathbf{E}(\mathbf{r}_\perp, z)$, then, by replacing the x and y components with the $\mathbf{P}(\mathbf{r}_\perp, z)$ and $\mathbf{Q}(\mathbf{r}_\perp, z)$ vector fields, we obtain the expressions for the new local Stokes parameters:

$$\begin{aligned}\tilde{S}_0(\mathbf{r}_\perp, z) &= \|\mathbf{P}(\mathbf{r}_\perp, z)\|^2 + \|\mathbf{Q}(\mathbf{r}_\perp, z)\|^2 \\ &= \|\mathbf{E}_r(\mathbf{r}_\perp, z)\|^2 + \|\mathbf{E}_i(\mathbf{r}_\perp, z)\|^2,\end{aligned} \tag{9a}$$

$$\begin{aligned}\tilde{S}_1(\mathbf{r}_\perp, z) &= \|\mathbf{P}(\mathbf{r}_\perp, z)\|^2 - \|\mathbf{Q}(\mathbf{r}_\perp, z)\|^2 \\ &= \frac{\|\mathbf{E}_r(\mathbf{r}_\perp, z)\|^2 - \|\mathbf{E}_i(\mathbf{r}_\perp, z)\|^2}{\cos 2\alpha(\mathbf{r}_\perp, z)},\end{aligned} \tag{9b}$$

$$\tilde{S}_2(\mathbf{r}_\perp, z) = 0, \tag{9c}$$

$$\begin{aligned}\tilde{S}_3(\mathbf{r}_\perp, z) &= 2\|\mathbf{N}(\mathbf{r}_\perp, z)\| = 2\|\mathbf{P}(\mathbf{r}_\perp, z) \times \mathbf{Q}(\mathbf{r}_\perp, z)\| \\ &= 2\|\mathbf{E}_r(\mathbf{r}_\perp, z) \times \mathbf{E}_i(\mathbf{r}_\perp, z)\|,\end{aligned} \tag{9d}$$

which involve information about all three components of the field. Furthermore, note that the dependence on $\mathbf{E}_r(\mathbf{r}_\perp, z)$ and $\mathbf{E}_i(\mathbf{r}_\perp, z)$ on the right-hand side of the last equality in all these expressions gives us a precise idea of how to relate the experimentally inferred field with the new Stokes parameters. Indeed, the fact that these new parameters contain information about both the amplitude and the phase of the three field components constitutes a challenge from an experimental point of view because a reliable method must be devised to extract such information. To cope with the task, we used a method based on imposing Gauss' law to the measured transverse field, which avoids unwanted direct interactions with an intermediate material medium. Further details on this experimental method are briefly accounted for in Appendix A.

So far, the formalism above has not been particularized to any specific type of field; in principle, it can be applied to any arbitrary field. Due to their intrinsic fundamental and technological interest, though, let us turn our attention to highly focused fields, taking them as a benchmark to compare the theory and experiment. Let us analyze the field arising from a monochromatic field incident on the entrance pupil of an aplanatic focusing system with a high NA. This focusing system is illustrated in Fig. 1, which shows the different reference coordinate systems and variables of interest. The highly focused field that results can be described, at the focal region, in terms of the so-called Richards–Wolf integral [42],

$$\begin{aligned}&\mathbf{E}(r, \phi, z) \\ &= A\int_0^{\theta_0}\int_0^{2\pi} \mathbf{E}_0(\theta, \varphi) e^{ikr\,\sin\theta\,\cos(\phi-\varphi)} e^{ikz\,\cos\theta}\,\sin\theta \mathrm{d}\theta\mathrm{d}\varphi,\end{aligned} \tag{10}$$

where (r, ϕ, z) denote the cylindrical coordinates in that region, while θ and φ represent, respectively, the polar and azimuthal angles at the reference Gaussian sphere. In this integral, the expression for the input vector angular spectrum reads as

$$\mathbf{E}_0(\theta, \varphi) = \sqrt{\cos\theta}[(\mathbf{E}_s \cdot \hat{\mathbf{e}}_1)\hat{\mathbf{e}}_1 + (\mathbf{E}_s \cdot \hat{\mathbf{e}}_2')\hat{\mathbf{e}}_2], \tag{11}$$

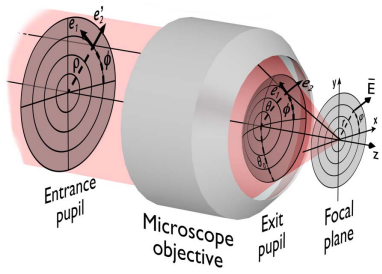

Fig. 1. Diagram of the focusing system (microscope objective) illustrating the reference coordinate systems and the variables involved in the process [44].

where $\mathbf{E}_s$ is the transverse field distribution at the entrance pupil, with the unit vectors defined as

$$\begin{aligned}\hat{\mathbf{e}}_1 &= \begin{pmatrix} -\sin\varphi \\ \cos\varphi \\ 0 \end{pmatrix}, \quad \hat{\mathbf{e}}_2 = \begin{pmatrix} \cos\theta\cos\varphi \\ \cos\theta\sin\varphi \\ -\sin\theta \end{pmatrix}, \\ \hat{\mathbf{e}}_2' &= \begin{pmatrix} \cos\varphi \\ \sin\varphi \\ 0 \end{pmatrix}.\end{aligned} \tag{12}$$

Specifically, $\hat{\mathbf{e}}_1$ and $\hat{\mathbf{e}}_2$ point, respectively, along the azimuthal and radial directions, while $\hat{\mathbf{e}}_2'$ is the projection of $\hat{\mathbf{e}}_2$ onto the entrance pupil plane. Regarding other parameters in the integral [Eq. (10)]: A is a constant, $k = 2\pi/\lambda$ is the wave number, and $\theta_0 = \max\{\theta\}$ is the semi-aperture angle when a numerical aperture $\mathrm{NA} = \sin\theta_0$ is considered.

As shown in Ref. [44], certain paraxial incident fields satisfy an uncertainty principle. This happens, for instance, when the transverse field distribution is

$$\mathbf{E}_s^{(X)}(\theta) = g(\theta)\hat{\mathbf{u}}_X, \tag{13}$$

where the subscript X denotes a generic polarization state (see below), and the amplitude $g(\theta)$ is given by the functional form

$$g(\theta) = \frac{e^{-\frac{\sigma}{2}\left(\frac{\cos\theta-\bar{\alpha}}{1-\cos\theta_0}\right)^2}}{\sqrt{\cos\theta}(1+\cos\theta)}, \tag{14}$$

with $\bar{\alpha}$ being a constant and σ controlling the width of the distribution [44]; see the blue solid line in Fig. 2. The polarization state is specified by the unit vector

$$\hat{\mathbf{u}}_X = \begin{pmatrix} \cos\bar{\theta}/2 \\ e^{i\bar{\varphi}}\sin\bar{\theta}/2 \end{pmatrix}, \tag{15}$$

where $0 \le \bar{\theta} \le \pi$ and $0 \le \bar{\varphi} < 2\pi$ to map all points on the Bloch sphere (isomorphic to the Poincaré one), as seen in Fig. 3. We specifically consider this notation because of the potential interest for the method in quantum optics and quantum technologies [45]. Denoting the Cartesian directions in this sphere arbitrarily by $\bar{x}$, $\bar{y}$, and $\bar{z}$, we follow the convention that the north and south poles (extrema along the $\bar{z}$ axis) correspond to horizontal and vertical polarization states ($X = H, V$), respectively, while the two circular polarization states ($X = R, L$) are on both extrema along the $\bar{y}$ axis ($\bar{\theta} = \pi/2$ and $\bar{\varphi} = \pi/2, 3\pi/2$). The third natural polarization basis, described by the diagonal and anti-diagonal polarization states ($X = D, A$), corresponds to both extrema along the $\bar{x}$ axis ($\bar{\theta} = \pi/2$ and $\bar{\varphi} = 0, \pi$). All other points on the sphere represent elliptical polarization states with different degrees of eccentricity.

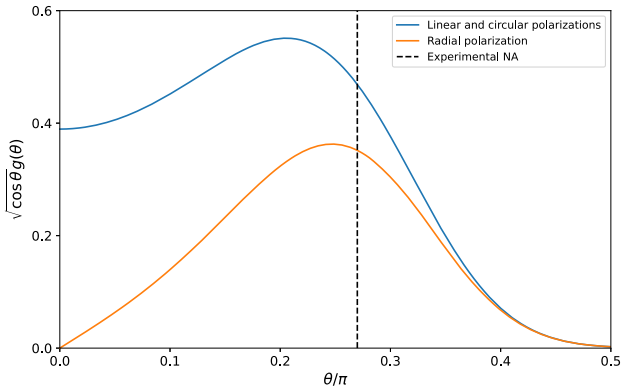

Fig. 2. Blue and orange solid lines represent the field amplitudes in, respectively, Eqs. (14) and (16) multiplied by the prefactor $\sqrt{\cos\theta}$, as it appears in Eq. (11). The vertical dashed line denotes the angular value associated with the numerical aperture considered here.

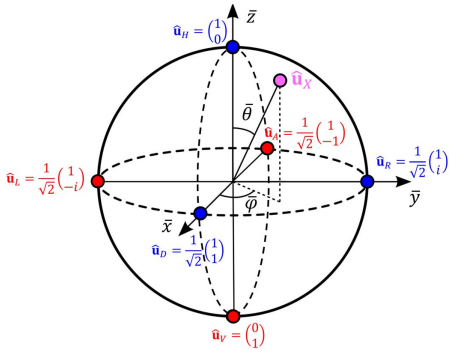

Fig. 3. Bloch sphere diagram illustrating the state of homogeneous polarization $\mathbf{u}_X$ [Eq. (15)]. Along the different axes are the six more representative elements of the three usual two-vector basis sets: $\{\mathbf{u}_H, \mathbf{u}_V\}$, $\{\mathbf{u}_D, \mathbf{u}_A\}$, and $\{\mathbf{u}_R, \mathbf{u}_L\}$.

The field above represents situations characterized by a uniform polarization at the input plane. It is thus interesting to also investigate the case of input fields with a nonuniform polarization state. This is the case of radially polarized fields, with a functional form like that of the field in Eq. (13), although its amplitude is slightly modified with a prefactor $\sin\theta$ to avoid the singularity at the origin; i.e.,

$$g(\theta) = \frac{\sin\theta e^{-\frac{\sigma}{2}\left(\frac{\cos\theta-\tilde{\alpha}}{1-\cos\theta_0}\right)^2}}{\sqrt{\cos\theta}(1+\cos\theta)}, \tag{16}$$

as shown by the orange solid line in Fig. 2, and with the polarization state being described by a unit vector depending on the azimuthal angle,

$$\hat{\mathbf{u}}_r = \begin{pmatrix} \cos\varphi \\ \sin\varphi \end{pmatrix}. \tag{17}$$

Let us now analyze these cases in more detail from a theoretical point of view before considering the corresponding experiments.

A. Linearly Polarized Input Fields

First, we consider an incident field with horizontal polarization [$\bar{\theta} = \bar{\varphi} = 0$ in Eq. (15)]:

$$\hat{\mathbf{u}}_I = \begin{pmatrix} 1 \\ 0 \end{pmatrix}. \tag{18}$$

The input vector angular spectrum is

$$\mathbf{E}_0^{(I)}(\theta,\varphi) = \frac{1}{2}\sqrt{\cos\theta}\,g(\theta)\begin{pmatrix} 1+\cos\theta+\cos 2\varphi(\cos\theta-1) \\ \sin\varphi(\cos\theta-1) \\ -2\sin\theta\cos\varphi \end{pmatrix}, \tag{19}$$

after substituting Eq. (13) into Eq. (11). With this angular spectrum, the Richards–Wolf integral in Eq. (10) renders

$$\mathbf{E}^{(I)}(r,\phi) = \begin{pmatrix} D_0(r)+\cos 2\phi\, D_2(r) \\ \sin 2\phi\, D_2(r) \\ -2i\cos\phi\, D_1(r) \end{pmatrix}, \tag{20}$$

which is an expression for the field at the focal plane ($z = 0$) and is a function of the auxiliary radial integrals

$$D_0(r) = \pi A\int_0^{\theta_0}\sqrt{\cos\theta}\,g(\theta)(1+\cos\theta)J_0(kr\sin\theta)\sin\theta\mathrm{d}\theta, \tag{21a}$$

$$D_1(r) = \pi A\int_0^{\theta_0}\sqrt{\cos\theta}\,g(\theta)\sin\theta J_1(kr\sin\theta)\sin\theta\mathrm{d}\theta, \tag{21b}$$

$$D_2(r) = \pi A\int_0^{\theta_0}\sqrt{\cos\theta}\,g(\theta)(1-\cos\theta)J_2(kr\sin\theta)\sin\theta\mathrm{d}\theta, \tag{21c}$$

with $J_n(kr\sin\theta)$ denoting the Bessel function of the first kind and order n. Note that the polarization state displayed by Eq. (20) is going to depend on the value acquired by these integrals at every point in the focal plane.

The dependence on r of these three integrals is shown in Fig. 4(a) for $\sigma = 2$ and NA $= 0.75$, which are the values also considered in the experiments here. We observed that the contribution from D_0 around the focal region (i.e., within the region $r \lesssim \lambda/2$) is much more prominent than the contributions arising from D_1 and, more particularly, D_2, which is almost negligible. In this sense, by inspecting Eq. (20), we noticed that, although the field polarization is seemingly highly nonuniform, in a good approximation we can say that the field is mainly polarized along the x direction, which is true for $\varphi = \pi/2$ or $3\pi/2$; i.e., along the direction $x = 0$. Nonetheless, because of the non-negligible contribution of D_1 around $r \sim \lambda/2$, there will be a slight trace of elliptical polarization contained within the plane XZ, although with eccentricity modulated by the azimuthal angle. Interestingly, if we compute the usual transverse Stokes parameters for this case, we obtain

$$S_0(r,\phi) = D_0^2(r) + D_2^2(r) + 2\cos 2\phi\, D_0(r)D_2(r), \tag{22a}$$

$$S_1(r,\phi) = D_0^2(r) + \cos 4\phi D_2^2(r) + 2\cos 2\phi\, D_0(r)D_2(r), \tag{22b}$$

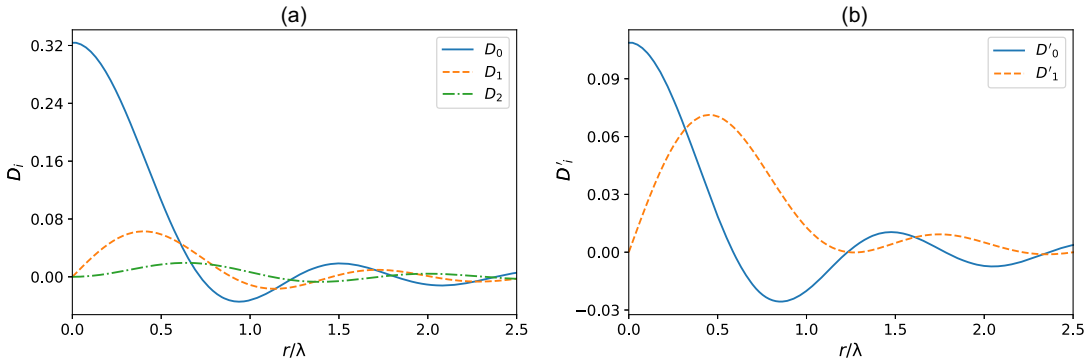

Fig. 4. (a) Representation of the D_i functions in Eq. (21), in terms of the radial distance r for $g(\theta)$ given by Eq. (14). D_0 is denoted with a solid blue line, D_1 with the dashed orange line, and D_2 with the dash-dotted green line. (b) Representation of the D'_i functions in Eq. (37), in terms of the radial distance r, for $g(\theta)$ given by Eq. (16). The solid blue line and the dashed orange line denote, respectively, D'_0 and D'_1.

$$S_2(r,\phi) = 2\sin 2\phi\, D_0(r)D_2(r) + \sin 4\phi\, D_2^2(r), \tag{22c}$$

$$S_3(r,\phi) = 0. \tag{22d}$$

According to these parameters, there is no trace of elliptical polarization. Rather, taking into account the relative weight of the different contributions, we find that the polarization state is essentially linear (horizontal), as $S_0 \approx S_1$, $S_2 \approx 0$, and $S_3 = 0$.

If we now apply our method, from the real and imaginary components of the field at the focal plane, we get

$$\mathbf{E}_r^{(l)}(r,\phi) = \begin{pmatrix} D_0(r) + \cos 2\phi\, D_2(r) \\ \sin 2\phi\, D_2(r) \\ 0 \end{pmatrix},$$
$$\mathbf{E}_i^{(l)}(r,\phi) = \begin{pmatrix} 0 \\ 0 \\ -2\cos\phi\, D_1(r) \end{pmatrix}, \tag{23}$$

which are already mutually orthogonal; hence $\mathbf{P}^{(l)}$ and $\mathbf{Q}^{(l)}$ can be directly identified with $\mathbf{E}_r^{(l)}$ and $\mathbf{E}_i^{(l)}$, respectively, as $\alpha(r) = 0$ for all values of r. Then, we obtain the normal vector

$$\mathbf{N}^{(l)}(r,\phi) = 2D_1(r)\cos\phi \begin{pmatrix} -\sin 2\phi\, D_2(r) \\ D_0(r) + \cos 2\phi\, D_2(r) \\ 0 \end{pmatrix}. \tag{24}$$

Except for minor contributions from its x component, around the focus where the irradiance mainly concentrates, this vector essentially points upward (toward positive y) for $x > 0$, and downward for $x < 0$, indicating that there is basically a single polarization plane, which coincides with the XZ plane in a good approximation, and where the field exhibits elliptical polarization; of course, with a prominent major axis oriented along the x direction. Along the direction $x = 0$, however, the normal vector cancels out; hence, the polarization state corresponds to linear horizontal polarization. This behavior is better seen in Fig. 5(a), where $\mathbf{N}^{(l)}$ is shown in the form of a vector plot, with the arrows representing this vector at different points of the focal plane being proportional to its corresponding modulus. To get an idea of the relevance of the field within the region, the arrow map is displayed superimposed to the density plot of the irradiance, which clearly shows that the relevant region where energy concentrates is on the order of $\lambda/2$ around the focus. This complies with the information provided by the local Stokes parameters, which read as

$$\tilde{S}_0(r,\phi) = D_0^2(r) + D_2^2(r) + 2\cos 2\phi\, D_0(r)D_2(r) + 4\cos^2\phi\, D_1^2(r), \tag{25a}$$

$$\tilde{S}_1(r,\phi) = D_0^2(r) + D_2^2(r) + 2\cos 2\phi\, D_0(r)D_2(r) - 4\cos^2\phi\, D_1^2(r), \tag{25b}$$

$$\tilde{S}_2(r,\phi) = 0, \tag{25c}$$

$$\tilde{S}_3(r,\phi) = 4|\cos\phi||D_1(r)|\sqrt{D_0^2(r) + D_2^2(r) + 2\cos 2\phi\, D_0(r)D_2(r)}. \tag{25d}$$

As it can readily be noticed, now we have a non-negligible parameter; namely $\tilde{S}_3$, which indicates that, to a certain extent, the field is elliptically polarized. Furthermore, again, except for a slight variation provoked by the term containing D_1^2, the two first local Stokes parameters, $\tilde{S}_0$ and $\tilde{S}_1$, are quite similar in value.

B. Circularly Polarized Input Fields

Let us now consider the case of circular polarization [$\tilde{\theta} = \pi/2$ and $\tilde{\varphi} = \pm\pi/2$ in Eq. (15)], where

$$\hat{\mathbf{u}}_c = \frac{1}{\sqrt{2}}\begin{pmatrix} 1 \\ \gamma i \end{pmatrix}, \tag{26}$$

with $\gamma = \pm 1$. The angular spectrum is

$$\mathbf{E}_0^{(c)}(\theta,\varphi) = \frac{g(\theta)}{2\sqrt{2}}\begin{pmatrix} 1 + \cos\theta + e^{\gamma 2i\varphi}(\cos\theta - 1) \\ \gamma i(1 + \cos\theta) - \gamma i e^{\gamma 2i\varphi}(\cos\theta - 1) \\ -2\sin\theta e^{\gamma i\varphi} \end{pmatrix}, \tag{27}$$

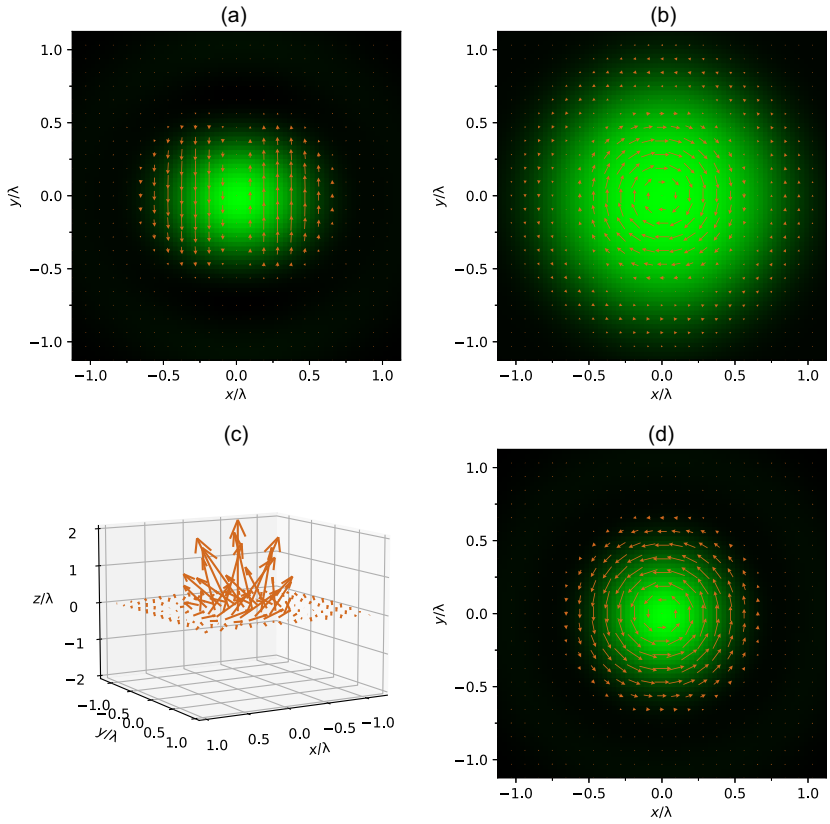

Fig. 5. Vector plots of the normal direction vector $\mathbf{N}^{(X)}(r,\phi)$ at the focal plane ($z=0$) for input fields with different polarization states. (a) Linear (horizontal) polarization in Eq. (24). (b) Radial polarization in Eq. (40). (c) and (d) Circular right-handed polarization in Eq. (33). A 3D picture is represented in panel (c), while panel (d) offers a 2D representation with only the transverse components of $\mathbf{N}^{(c)}(r,\phi)$. In panels (a), (b), and (d) a density plot of the irradiance at the focal plane is also provided to have an idea of the spatial region where the field energy is mainly concentrated. The color scale, from black to light green, indicates the increasing value of the irradiance. In these calculations, $\sigma=2$ and NA $=0.75$, as in the experiments.

while the field at the focal plane is

$$\mathbf{E}^{(c)}(r,\phi)=\begin{pmatrix} D_0(r)+e^{\gamma 2i\phi}D_2(r)\\ \gamma i D_0(r)-\gamma i e^{\gamma 2i\phi}D_2(r)\\ -2ie^{\gamma i\phi}D_1(r)\end{pmatrix}. \tag{28}$$

Again, the field polarization is seemingly highly nonuniform, except at the origin ($r=0$), where it has the same polarization as the input field. Now, if we proceed as before, and consider the dependence on r of the auxiliary integrals, as shown in Fig. 4(a), we notice that this polarization state, except for minor corrections, extends to the whole focal plane. This is also seen from the corresponding transverse Stokes parameters

$$S_0(r,\phi)=2[D_0^2(r)+D_2^2(r)], \tag{29a}$$

$$S_1(r,\phi)=4\cos 2\phi D_0(r)D_2(r), \tag{29b}$$

$$S_2(r,\phi)=4\sin 2\phi D_0(r)D_2(r), \tag{29c}$$

$$S_3(r,\phi)=2\gamma[D_0^2(r)-D_2^2(r)], \tag{29d}$$

where, in a first approximation, we have $S_3\approx\gamma S_0$, while $S_1\approx S_2\approx 0$, which corresponds to circular polarization, with γ determining the handedness, just like in the case of the input field. Again, however, the question is: what is the role played by the third (z) component of the field in Eq. (28)?

As before, from the real and imaginary components of the field in Eq. (28), we get

$$\mathbf{E}_r^{(c)}(r,\phi)=\begin{pmatrix} D_0(r)+\cos 2\phi D_2(r)\\ \sin 2\phi D_2(r)\\ \gamma 2\sin\phi D_1(r)\end{pmatrix},$$

$$\mathbf{E}_i^{(c)}(r,\phi)=\begin{pmatrix} \gamma\sin 2\phi D_2(r)\\ \gamma D_0(r)-\gamma\cos 2\phi D_2(r)\\ -2\cos\phi D_1(r)\end{pmatrix}, \tag{30}$$

from which the $\mathbf{P}$ and $\mathbf{Q}$ vectors are determined by

$$\mathbf{P}^{(c)}(r,\phi)=[D_0(r)+D_2(r)]\begin{pmatrix}\cos\phi\\ \sin\phi\\ 0\end{pmatrix}, \tag{31}$$

$$\mathbf{Q}^{(c)}(r,\phi)=[D_0(r)-D_2(r)]\begin{pmatrix}-\gamma\sin\phi\\ \gamma\cos\phi\\ -\frac{2D_1(r)}{D_0(r)-D_2(r)}\end{pmatrix}, \tag{32}$$

with $\alpha=\gamma\phi$. While $\mathbf{P}^{(c)}$ is fully contained within the focal plane, notice that $\mathbf{Q}^{(c)}$ points outward; only at the focus,

$\mathbf{Q}^{(c)}$ is also fully contained within the focal plane. As for the normal vector, it is

$$\mathbf{N}^{(c)}(r,\phi) = 2[D_0(r) + D_2(r)]D_1(r)\begin{pmatrix} -\sin\phi \\ \cos\phi \\ \frac{\gamma[D_0(r)-D_2(r)]}{2D_1(r)} \end{pmatrix}, \quad (33)$$

which, in general, will point out of the focal plane toward positive z for right-handed polarization, and to negative z for left-handed polarization. A 3D representation of this vector for right-handed polarization is shown in Fig. 5(c) to illustrate this behavior. Regarding the transverse components of $\mathbf{N}^{(c)}$ that remain within the (XY) focal plane, we note from Eq. (33) that, in the region of interest (i.e., for $r \lesssim \lambda$), the corresponding 2D vectors will be oriented counterclockwise, describing a kind of left-handed whirlpool, as seen in Fig. 5(d). In this regard, it is important not to confuse the orientation of the normal vector with the handedness of the polarization state. Nonetheless, it is more remarkable that those 3D arrows specify locally (i.e., at each point on the focal plane) the direction normal to the planes that contain the polarization state of the field, which happens to be elliptical, as inferred from the expression of the local Stokes parameters

$$\tilde{S}_0(r,\phi) = 2[D_0^2(r) + 2D_1^2(r) + D_2^2(r)], \quad (34a)$$

$$\tilde{S}_1(r,\phi) = 4[D_0(r)D_2(r) - D_1^2(r)], \quad (34b)$$

$$\tilde{S}_2(r,\phi) = 0, \quad (34c)$$

$$\tilde{S}_3(r,\phi) = 2|D_0(r) + D_2(r)|\sqrt{[D_0(r) - D_2(r)]^2 + 4D_1^2(r)}. \quad (34d)$$

C. Radially Polarized Input Fields

Finally, we considered an input field with radial polarization,

$$\hat{\mathbf{u}}_r = \begin{pmatrix} \cos\phi \\ \sin\phi \end{pmatrix}, \quad (35)$$

as an example of a situation where the input polarization state is not uniform. In this case, the field at the focal plane is

$$\mathbf{E}^{(r)}(r,\phi) = \begin{pmatrix} i\cos\phi D_1'(r) \\ i\sin\phi D_1'(r) \\ -D_0'(r) \end{pmatrix}, \quad (36)$$

with the auxiliary integrals

$$D_0'(r) = \pi A\int_0^{\theta_0}\sqrt{\cos\theta}\,g(\theta)\sin\theta J_0(kr\sin\theta)\sin\theta \mathrm{d}\theta, \quad (37a)$$

$$D_1'(r) = \pi A\int_0^{\theta_0}\sqrt{\cos\theta}\,g(\theta)\cos\theta J_1(kr\sin\theta)\sin\theta \mathrm{d}\theta. \quad (37b)$$

These integrals are plotted against the radial distance r in Fig. 4(b) for the same experimental conditions. Unlike previous auxiliary integrals, now the contribution from both D_0' and D_1' is analogous within a region of the order of $r \lesssim \lambda$. Hence, any approximation must be carefully considered. Nonetheless, considering the dependence on r for D_0' and D_1' shown in Fig. 4(b), we can extract some conclusions regarding the polarization of the field in Eq. (36). In general, we find that it is elliptically polarized, with a relatively important contribution in the z direction; that is, out of the focal plane. At some values for r, for instance, the focus and other values at which D_1' cancels out (e.g., $r \approx 2.5\lambda$), the field becomes linearly polarized along the z direction. On the other hand, at those radial distances where D_0' vanishes (e.g., $r \approx 0.6\lambda$ or $r \approx 1.7\lambda$), the field will be radially polarized, like the input field. There also are other regions where D_0' and D_1' are both nearly zero (e.g., $r \approx 1.2\lambda$); hence, there is no field. All these behaviors, however, cannot be identified by only inspecting the transverse Stokes parameters, which are

$$S_0(r,\phi) = D_1'^2(r), \quad (38a)$$

$$S_1(r,\phi) = \cos 2\phi D_1'^2(r), \quad (38b)$$

$$S_2(r,\phi) = \sin 2\phi D_1'^2(r), \quad (38c)$$

$$S_3(r,\phi) = 0. \quad (38d)$$

Instead, the information provided by these parameters only refers to linear polarization (along the radial direction).

Contrary to that situation, we can see that the method introduced here is able to provide full information about the local polarization state of the field, even if we look at the (transverse) focal plane. As in the case of linear polarization,

$$\mathbf{E}_r^{(r)}(r,\phi) = D_0'(r)\begin{pmatrix} 0 \\ 0 \\ -1 \end{pmatrix},$$

$$\mathbf{E}_i^{(r)}(r,\phi) = D_1'(r)\begin{pmatrix} \cos\phi \\ \sin\phi \\ 0 \end{pmatrix}, \quad (39)$$

which are the real and imaginary components of the field in Eq. (36) that can be identified directly with, respectively, the $\mathbf{P}$ and $\mathbf{Q}$ vectors. This implies that the planes containing the vibrating field at each point of the focal plane will be perpendicular to this latter plane, as indicated by the associated normal vector

$$\mathbf{N}^{(r)}(r,\phi) = D_0'(r)D_1'(r)\begin{pmatrix} \sin\phi \\ -\cos\phi \\ 0 \end{pmatrix}. \quad (40)$$

There is an important difference, though, with the linear case: this normal vector rotates clockwise, while in the situation with linear polarization it was nearly parallel (in a good approximation) to the y axis. Of course, whenever D_0', D_1', or both vanish, the polarization state will be linear along the z axis, or there simply will not be polarization because there is no field. In any other case, the field will display an elliptical polarization, as also inferred from the expression of the corresponding local Stokes parameters

$$\tilde{S}_0(r,\phi) = D_0'^2(r) + D_1'^2(r), \quad (41a)$$

$$\tilde{S}_1(r,\phi) = D_0'^2(r) - D_1'^2(r), \quad (41b)$$

$$\tilde{S}_2(r,\phi) = 0, \tag{41c}$$

$$\tilde{S}_3(r,\phi) = 2|D_0'(r)D_1'(r)|. \tag{41d}$$

3. EXPERIMENTAL RESULTS

We checked the validity and reliability of the method by carrying out a series of experimental measures on highly focused fields prepared from input fields with particular irradiance distributions and definite polarization states, as described in Section 2 (Theory). The experimental procedure to produce these fields is described in Appendix A. From the amplitude and phase of the field components obtained from experimental measures at the focal plane, we have inferred the value of both the usual transverse Stokes parameters, using Eq. (9), and the local Stokes parameters, using the expressions on the right-hand side of the second equality in Eq. (8). In all the experiments, the input beams have been produced with $\sigma = 2$ and the focusing optical systems had NA = 0.75.

A. Linearly Polarized Input Field

The transverse Stokes parameters for an input field linearly polarized, with its angular spectrum described by Eq. (19), are displayed in the upper row in Fig. 6. As it can readily be noticed, they agree with the corresponding theoretical results in Eq. (22). Both S_0 and S_1 exhibit the seemingly circular symmetry that arises from the fact that D_0 is much larger than the other two contributing integrals, which, in turn, produces $S_0 \approx S_1 \approx D_0^2(r)$. On the other hand, $S_2 \approx 0$ because it depends linearly on D_2 and hence one expects this parameter to be nearly zero. Even though some faint structure can still be perceived, if we consider the scale bar on the right, we notice that the values are negligible. In the case of S_3, its value is not strictly zero, in compliance with Eq. (22d), but it enters within the accuracy limits associated with the experiment (sensitivity to misalignment and errors carried in the inference procedure). Therefore, according to these experimental data, we can conclude that the field is basically linearly polarized on the transverse (focal) plane, with the same direction as the incident field; that is, horizontal.

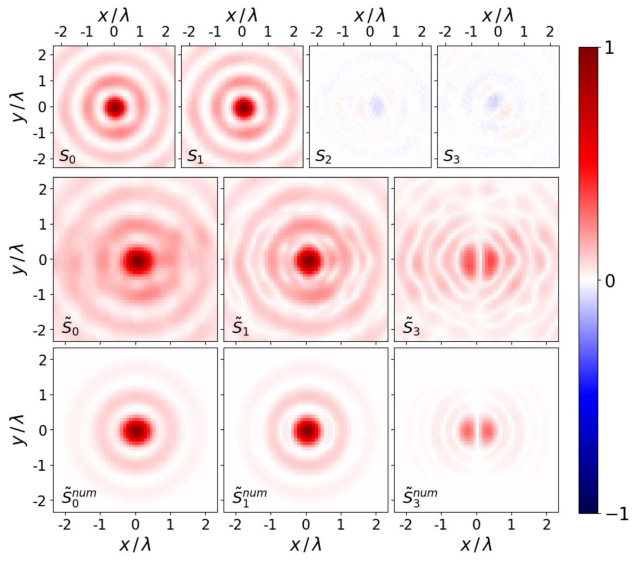

Fig. 6. Experimental value obtained for the transverse Stokes parameters (top row) and local Stokes parameters (middle row) at the focal plane for a linearly polarized input field, with horizontal polarization. The local Stokes parameters obtained numerically are shown in the bottom row of the figure for comparison. The color code on the right-hand side applies to all the panels. The input beam has been produced with $\sigma = 2$ and the focusing optical system has NA = 0.75.

If we now consider the local Stokes parameters, shown in the middle row of Fig. 6 ($\tilde{S}_2$ is not represented, because it is strictly zero by definition), we find that they effectively provide us with more information. In compliance with Eq. (25), first, we notice that both $\tilde{S}_0$ and $\tilde{S}_1$ also display a nearly circular symmetry due to the importance of the integral D_0 and, accordingly, $\tilde{S}_0 \approx \tilde{S}_1 \approx D_0^2(r)$. Second, not only $\tilde{S}_3$ is nonzero, but its value is relevant compared to the values of $\tilde{S}_0$ and $\tilde{S}_1$ (see the color bar on the right-hand side in Fig. 6), which denotes that there is an important contribution to the polarization going out of the plane across some regions of the focal plane. In particular, this non-homogeneity in the polarization state is described, in a good approximation, by the relation $\tilde{S}_3 \approx 4|\cos\phi D_1(r)D_0(r)|$. In those cases where $\tilde{S}_3$ is not zero, the polarization state is elliptical; otherwise, it will be linear and contained within the focal plane. Third, there is an excellent agreement with the theoretical values, as seen when we compare it to the panels of the bottom row of Fig. 6. It should be clarified, in this regard, that the fact that the rings in the numerical values are much fainter than in the experimental counterparts is related to the detection process, in which low intensity regions are often overestimated.

B. Circularly Polarized Input Field

The transverse Stokes parameters for an input field with right-handed polarization, with its angular spectrum being described by Eq. (27), are represented in the upper row in Fig. 7. Again, we find a good agreement with the corresponding theoretical results in Eq. (29), where now both S_0 and S_3 exhibit a nearly circular symmetry because their value is, except for minor deviations, close to $D_0^2(r)$, while both S_1 and S_2 are nearly zero due to their linear dependence on $D_2(r)$. Of course, they are not totally zero because of the small but finite value of $D_2(r)$, as seen in the color bar on the right-hand side of Fig. 7. Therefore, these experimental data show that the polarization state, within the transverse (focal) plane is basically circular with right handedness, except for minimal, second- or third-order deviations. In this regard, the polarization state is pretty close to that of the input field.

In the case of the local Stokes parameters, as shown in the middle row in Fig. 7, we find an analogous behavior, with $\tilde{S}_0 \approx \tilde{S}_3 \approx 2D_0^2(r)$ and $\tilde{S}_1 \approx 0$ in a good approximation, in compliance with Eq. (34). Of course, there are also some minor corrections that must be considered, but we essentially observe that, again, there is a good correspondence with the theoretical expectation. Note, however, that $\tilde{S}_1$ is not exactly zero, although its value all over the region is rather low. We can then conclude that, as it happens with the corresponding transverse Stokes parameters, the polarization state is circular, although we

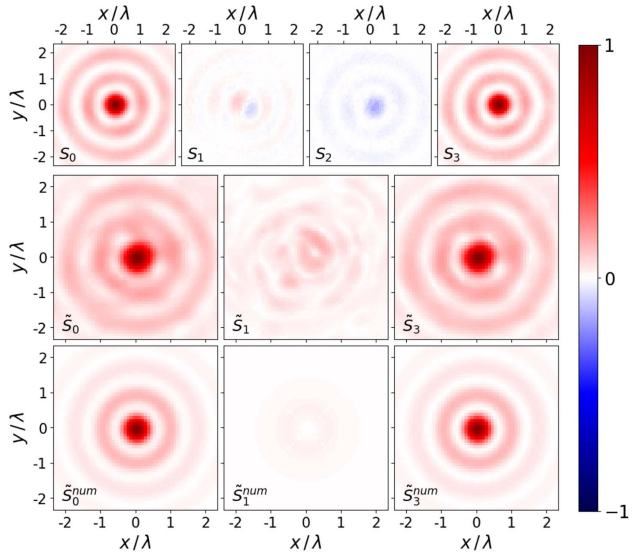

Fig. 7. Experimental value obtained for the transverse Stokes parameters (top row) and local Stokes parameters (middle row) at the focal plane for a circularly polarized input field, with right-handed polarization ($\gamma = +1$). The local Stokes parameters obtained numerically are shown in the bottom row of the figure for comparison. The color code on the right-hand side applies to all the panels. The input beam has been produced with $\sigma = 2$ and the focusing optical system has NA $= 0.75$.

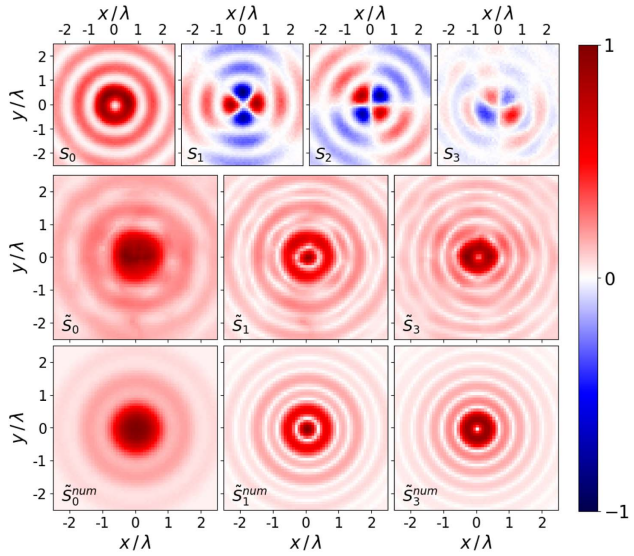

Fig. 8. Experimental value obtained for the transverse Stokes parameters (top row) and local Stokes parameters (middle row) at the focal plane for a radially polarized input field. The local Stokes parameters obtained numerically are shown in the bottom row of the figure for comparison. The color code on the right-hand side applies to all the panels. The input beam has been produced with $\sigma = 2$ and the focusing optical system has NA $= 0.75$.

can say nothing about the handedness, because $\tilde{S}_3$ is always a positive quantity. However, it is here where we find a major difference with respect to the usual transverse Stokes parameters, as already mentioned in Section 2 (Theory): this polarization state is, with respect to a locally defined normal direction vector that, for circular polarization, goes out of the focal plane, as specified by Eq. (33). It is the direction of its z component, forward or backward (with respect to the focal plane), what specifies the handedness of the polarization state because this component is proportional to the handedness factor γ. It therefore shows that the method requires both the local Stokes parameters and the normal vector. Both elements provide us with full 3D information about the polarization state of the field at a given point (i.e., locally), even if, as in a case like this, we are confined within a 2D plane.

C. Radially Polarized Input Field

Finally, the experimental data for a radially polarized input field are shown in Fig. 8. The transverse Stokes parameters are shown in the top row. We observe an excellent agreement between the experimental values and the theoretical ones, accounted for by Eq. (38), particularly in the case of S_0, S_1, and S_2, with all of them displaying the symmetries described by the corresponding analytical expressions. In the case of S_3 we find some discrepancies, which should vanish, according to Eq. (38d). This is only a spurious artifact due to misalignment and errors carried along its inference from the raw experimental data. So, all in all, these values show that the field, on the focal plane, is also radially polarized, like the input field.

The picture rendered by the local Stokes parameters, though, is a bit different: it captures the fact that the field has also a polarization component perpendicular to the focal plane. The middle row in Fig. 8 shows the local Stokes parameters for this case. The results agree very nicely with the theoretical expectations, described by Eq. (41), where both $D_0'(r)$ and $D_1'(r)$ have a major contribution, unlike the integrals involved in the linearly or circularly polarized states, where $D_0(r)$ has the leading role. More importantly, unlike the transverse Stokes parameters, which depend linearly only on $D_1'(r)$, in the local counterparts the two integrals make an important contribution. By inspecting the result obtained with both $\tilde{S}_1$ and $\tilde{S}_3$ being relevant, we conclude that the polarization state will, in general, be elliptical instead of radial. This is a rather counterintuitive result, which might lead us to ask why there is no radial polarization in a case where the input field is spatially characterized by a non-homogeneous polarization state. The answer is simple and has to do with the fact, as mentioned in Section 2 (Theory), that within this 3D picture, the input radial polarization has become an elliptical polarization within a plane perpendicular to the observation (focal) one, where the radial direction now determines one of the semiaxes of the corresponding polarization ellipse (the other axis will be parallel to the z axis). Note that the plane containing the polarization ellipse is now given by the normal vector in Eq. (41), which rotates clockwise with the azimuthal angle ϕ.

4. DISCUSSION

Motivated by the need to find a relatively simple but physically insightful method to specify the polarization state at a local level of 3D fields, particularly in the case of highly focused fields due to the relevance of the longitudinal component, we introduced a set of so-called local Stokes parameters. Unlike the usual

transverse Stokes parameters, computed on the plane perpendicular to the longitudinal field direction, the local ones are referred locally to the normal, to a plane determined by a basis set that contains the real and imaginary parts of the analyzed electric field; formally, the Argand–Gauss plane defined by the directions denoted by those two components. This allowed us to keep track of the 3D nature of the field because all the three field components are involved in the calculation of these parameters, unlike the usual transverse Stokes parameters, where the information provided by one of the field components is lost. In other words, although the transverse Stokes parameters do not discriminate information concerning the field z component when they are computed within a given (transverse) plane, the local Stokes parameters always contain information about all components at each point on that plane. This information is supplemented by the normal vector that determines the orientation of the plane the local Stokes parameters are referred to. Indeed, although any trace on the field helicity disappears from these Stokes parameters, it appears encoded in the directionality of the normal vector.

To further investigate the usefulness and potential reach of the newly defined local Stokes parameters, a series of benchmark experiments were carried out that compared the information provided by transverse and local Stokes parameters side-by-side. This was done for highly focused fields, obtained from input fields with three different polarization states: linear polarization, circular polarization, and radial polarization. Although the polarization state is relatively nonuniform, the high-focusing experimental conditions considered render interesting conclusions. For instance, note that while the field should be considered as linearly polarized across the focal plane according to the usual transverse Stokes parameters, there is a certain ellipticity in planes that perpendicularly cross the focal plane, as it is inferred from the corresponding local Stokes parameters. On the other hand, in the case of circular polarization, although both types of parameters provide a seemingly identical conclusion (namely, that the field is also circularly polarized at the focal plane), we noticed that the circular polarization described by the local Stokes parameters is referred to planes that intersect the focal plane and rotate according to the helicity of the input field. We also explored the situation with a radially polarized input field as an example of a nonhomogeneously polarized field, finding that the resulting field is elliptically polarized in planes perpendicular to the focal one and rotating around the focus. Notice in all these cases the remarkable influence of the local value of the field z component, which determined the reference oscillation plane, information that is totally missed in the case of the transverse Stokes parameters.

Last, but not least, we would like to stress the fact that, to some extent, some physical meaning has been associated with both the real and the imaginary components of the analyzed field, although typically only the real part is considered. Although this already goes far beyond the scope of the current work, it is still noteworthy that analogous analyses have recently be published that stress the relevance of the complex nature of optical fields from a physical point of view [46]; i.e., putting the complex nature of these fields at a level beyond the widespread use as a bare mathematical artifact.

APPENDIX A: MATERIALS AND METHODS

1. Experimental Setup

The fields considered here have been experimentally generated using an optical setup suitable to produce highly focused fields, as shown in Fig. 9. In brief, a fiber-coupled laser (LP520-SF15 at 520 nm, Thorlabs) is collimated by means of an L1 lens. This field illuminates a translucent twisted-nematic liquid crystal device (TN-LCD) (HEO 0017, Holoeye Photonics) able to modulate both the amplitude and the phase of the wavefront. Polarizer LP1 and quarter-wave plate QWP1 configure the LCD in such a way that a phase-mostly configuration is fulfilled. The information required to produce a specific field is encoded on the LCD using the double-pixel hologram approach [47]. Then, the modulated wavefront passes through polarizer LP2, and, depending on the problem considered, an extra polarizing element should be included: a quarter-wave plate QWP2 is used for circularly or elliptically polarized light whereas a vortex retarder (VR) is used to produce radial, azimuthal, or spiral polarization. The LCD is imaged on the entrance pupil of microscope objective MO1 (N40X-PF Nikon Plan Fluorite with $NA_1 = 0.75$) by means of relay lenses L2 and L3. A spatial filter (SF), placed in the back focal plane of L2, removes diffracted terms generated by the hologram.

The microscope objective MO2, which is identical to MO1, images the light distribution produced by MO1 on a CCD camera (Stingray with a 14-bit depth and a pixel pitch of 3.75 μm). The position of the camera is controlled by a motorized tool (LTA-HL, Newport) with a unidirectional repeatability of ±100 nm. Finally, a quarter-wave plate QWP3 and a polarizer LP3 are used to record the polarimetric images necessary to generate the Stokes parameters.

We have experimentally investigated the polarization state at the focal plane resulting from three input fields with well-defined (input) polarization states: namely, linear, circular, and radial polarization. In the three cases, we chose the value $\sigma = 2$ for the parameter ruling the width of the transverse field distribution [see Eqs. (14) and (16)] and a numerical aperture

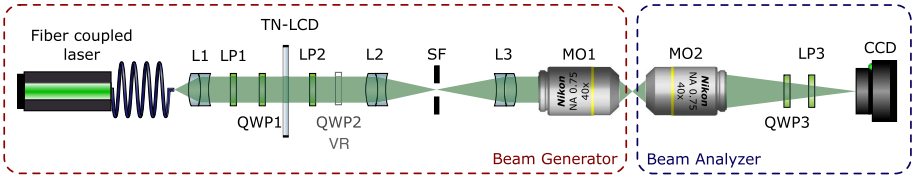

Fig. 9. Experimental setup (see the main text for details). To produce a linearly polarized input field, QWP2 is removed, while it is replaced by the VR if radially, azimuthally, or spirally polarized input fields are required.

NA = 0.75. Furthermore, for comparison, in all cases we represented both the usual transverse Stokes parameters and the newly defined local Stokes ones. Regarding the latter case, both the values inferred from experimental measures and their corresponding numerical estimates have been plotted, as shown by Figs. 6–8.

2. Experimental Data Processing

The experimental setup shown in Fig. 9 makes it possible to obtain irradiance images of the transverse field around the focal zone. However, the three complex amplitudes of the electric field (E_x, E_y, E_z) should be known in advance to determine the local Stokes distributions. In this section, we describe a method to retrieve the total field using the transverse components. This technique is fully described in Ref. [43] and consists of several steps that are illustrated in Fig. 10 and detailed below. The determination of the three components of the field is carried out without interacting with any medium. Our approach provides a fair estimation of the current longitudinal component by just manipulating the transverse one. Interestingly, it does not require the use of more complex techniques such as knife-edge scanning or near-field optical microscopy [25,48]. Here are the steps.

- **Experimental polarimetric images.** In the first step, we record the polarimetric information associated with the transverse components of the field in two different planes (front and back) around the focus, using a CCD camera. The positions of both the front plane (z_F) and the back plane (z_B) are separated at a distance equal to 2 μm. Even though the knowledge of the exact position of the focal plane $z = 0$ is not required, the following conditions should hold: $z_B < 0$ and $z_F > 0$. We record the six polarimetric images (I_0^F, I_{45}^F, I_{90}^F, I_{135}^F, I_R^F, and I_L^F) using linear polarizer LP3 and quarter-wave plate QWP3. Then, the experimental phase shift δ between the x and y components of the front plane is calculated using S_2^F and S_3^F.
- **Transverse phase retrieval.** The phase of the x and y components is recovered independently using Fienup's iterative method [49]. This phase retrieval algorithm is based on computationally propagating the experimental field moduli between the back and front planes, with a random phase initialization. Forward and backward free space propagations are performed between the back and front planes. At each step, the computed amplitude is replaced with the experimental one. Once the mean squared error between the experimental and computationally retrieved moduli reaches a prescribed value, or the algorithm has iterated a certain number of times, the phases of each electromagnetic field component are considered to be estimated. An acceleration method is used to improve the convergence rate as well as to avoid local minima in the process.
- **Set the phase shift.** Note that the retrieved phase is referenced to an arbitrary initial phase value, which is different for both the x and y components: it depends solely on the random initialization of the algorithm and does not separately affect the propagation of each component. Nevertheless, the phase shift at each point is related to the particular polarization state of the field.

The arbitrary initial phase is determined in this way: for each polarization component, we select the phase of the point with the highest transverse irradiance of the field ($\mathbf{r}_0$) and then globally subtract this phase value from all the points of the corresponding phase distribution. In this way, the phase at $\mathbf{r}_0$ is zero for both components. Finally, we globally add the experimental phase shift $\delta(\mathbf{r}_0)$ to the y polarization component.

- **Estimation of the position of the focal plane.** Once the complex transverse electromagnetic field at a certain plane is known, it can be propagated to any other using the Fresnel diffraction formula. To estimate the position of the focal plane, we scanned the transverse irradiance between the back and front planes. Then, the plane with a maximum density irradiance contains the focal point.
- **Longitudinal component retrieval.** To retrieve the longitudinal component of the field, we take advantage of Gauss' law, which in the present context reduces to

$$\nabla \cdot \mathbf{E}(\mathbf{r}) = 0. \tag{A1}$$

After some algebraic manipulations, which include recasting the transverse field in terms of its angular spectrum at the focal

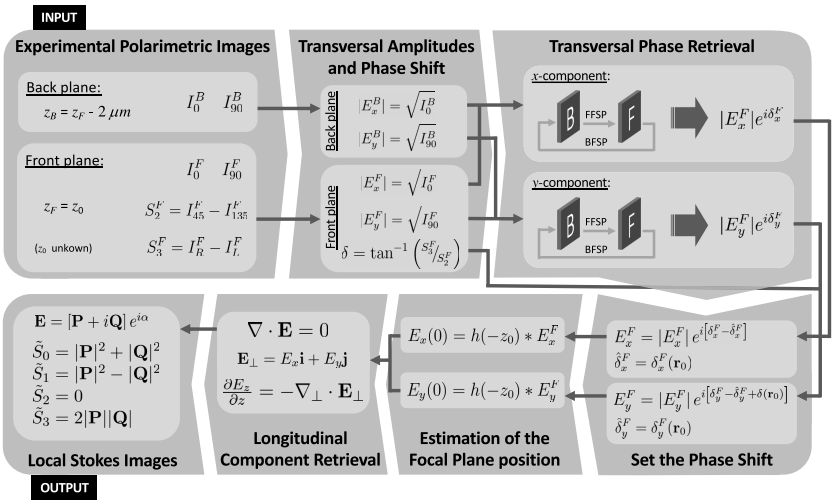

Fig. 10. Experimental data management pipeline. See the main text for a detailed explanation of each processing block. FFSP, forward free space propagation; BFSP, backward free space propagation; $h(\cdot)$, the convolution kernel of the Fresnel diffraction; and $*$, the convolution product.

plane and then integrating it over the z coordinate, we finally get

$$E_z(\mathbf{r}) = -\frac{1}{4\pi^2}\int_{k_\perp^2 \le k^2} \frac{\mathbf{k}_\perp \cdot \hat{\mathbf{E}}_\perp(\mathbf{k}_\perp, z=0)}{k_z} e^{ik_z z} e^{i\mathbf{k}_\perp \cdot \mathbf{r}} \mathrm{d}\mathbf{k}_\perp, \tag{A2}$$

where $\mathbf{k}_\perp = (k_x, k_y)$ and k_z is the transverse and longitudinal wave vectors, respectively, satisfying $k^2 = k_\perp^2 + k_z^2$. $\hat{\mathbf{E}}_\perp$ is the plane wave spectrum of the transverse component. Once both the amplitude and phase of the three components of the field are obtained, the local Stokes images can be directly computed by Eq. (9).

Funding. Ministerio de Ciencia e Innovación (PID2019-104268GB-C21, PID2019-104268GB-C22, PID2021-127781NB-I00).

Disclosures. The authors declare no conflicts of interest.

Data Availability. Data underlying the results presented in this paper are not publicly available at this time but may be obtained from the authors upon reasonable request.

REFERENCES

1. K. Y. Bliokh and F. Nori, "Transverse and longitudinal angular momenta of light," Phys. Rep. **592**, 1–38 (2015).
2. B. A. Knyazev and V. G. Serbo, "Beams of photons with nonzero projections of orbital angular momenta: new results," Phys. Usp. **61**, 449–479 (2018).
3. A. V. Andreev, O. A. Shoutova, S. M. Trushin, and S. Y. Stremoukhov, "3D Stokes parameters for vector focal fields," J. Opt. Soc. Am. B **39**, 1775–1782 (2022).
4. E. Jera, S. Zhou, and Q. Zhan, "Generation of three-dimensionally homogenized focal spot with uniform intensity distribution using vectorial optical fields," Opt. Commun. **464**, 125530 (2020).
5. A. Forbes, M. de Oliveira, and M. R. Dennis, "Structured light," Nat. Photonics **15**, 253–262 (2021).
6. D. Maluenda, R. Martínez-Herrero, I. Juvells, and A. Carnicer, "Synthesis of highly focused fields with circular polarization at any transverse plane," Opt. Express **22**, 6859–6867 (2014).
7. D. P. Biss and T. G. Brown, "Polarization-vortex-driven second-harmonic generation," Opt. Lett. **28**, 923–925 (2003).
8. C. J. R. Sheppard and A. Choudhury, "Annular pupils, radial polarization, and superresolution," Appl. Opt. **43**, 4322–4327 (2004).
9. Y. Gorodetski, A. Niv, V. Kleiner, and E. Hasman, "Observation of the spin-based plasmonic effect in nanoscale structures," Phys. Rev. Lett. **101**, 043903 (2008).
10. L. T. Vuong, A. J. L. Adam, J. M. Brok, P. C. M. Planken, and H. P. Urbach, "Electromagnetic spin-orbit interactions via scattering of subwavelength apertures," Phys. Rev. Lett. **104**, 083903 (2010).
11. A. Carnicer, I. Juvells, B. Javidi, and R. Martínez-Herrero, "Optical encryption in the longitudinal domain of focused fields," Opt. Express **24**, 6793–6801 (2016).
12. Q. Zhan, "Properties of circularly polarized vortex beams," Opt. Lett. **31**, 867–869 (2006).
13. C. Maurer, A. Jesacher, S. Fürhapter, S. Bernet, and M. Ritsch-Marte, "Tailoring of arbitrary optical vector beams," New J. Phys. **9**, 78 (2007).
14. X.-L. Wang, Y. Li, J. Chen, C.-S. Guo, J. Ding, and H.-T. Wang, "A new type of vector fields with hybrid states of polarization," Opt. Express **18**, 10786–10795 (2010).
15. X.-L. Wang, J. Ding, W.-J. Ni, C.-S. Guo, and H.-T. Wang, "Generation of arbitrary vector beams with a spatial light modulator and a common path interferometric arrangement," Opt. Lett. **32**, 3549–3551 (2007).
16. I. Moreno, C. Iemmi, J. Campos, and M. J. Yzuel, "Jones matrix treatment for optical Fourier processors with structured polarization," Opt. Express **19**, 4583–4594 (2011).
17. D. Maluenda, I. Juvells, R. Martínez-Herrero, and A. Carnicer, "Reconfigurable beams with arbitrary polarization and shape distributions at a given plane," Opt. Express **21**, 5432–5439 (2013).
18. E. H. Waller and G. von Freymann, "Independent spatial intensity, phase and polarization distributions," Opt. Express **21**, 28167–28174 (2013).
19. W. Han, Y. Yang, W. Cheng, and Q. Zhan, "Vectorial optical field generator for the creation of arbitrarily complex fields," Opt. Express **21**, 20692–20706 (2013).
20. R. Martínez-Herrero, I. Juvells, and A. Carnicer, "On the physical realizability of highly focused electromagnetic field distributions," Opt. Lett. **38**, 2065–2067 (2013).
21. C.-S. Guo, Z.-Y. Rong, and S.-Z. Wang, "Double-channel vector spatial light modulator for generation of arbitrary complex vector beams," Opt. Lett. **39**, 386–389 (2014).
22. Z.-Y. Rong, Y.-J. Han, S.-Z. Wang, and C.-S. Guo, "Generation of arbitrary vector beams with cascaded liquid crystal spatial light modulators," Opt. Express **22**, 1636–1644 (2014).
23. R. Martínez-Herrero, D. Maluenda, I. Juvells, and A. Carnicer, "Synthesis of light needles with tunable length and nearly constant irradiance," Sci. Rep. **8**, 2657 (2018).
24. L. Novotny, M. R. Beversluis, K. S. Youngworth, and T. G. Brown, "Longitudinal field modes probed by single molecules," Phys. Rev. Lett. **86**, 5251–5254 (2001).
25. A. Bouhelier, M. R. Beversluis, and L. Novotny, "Near-field scattering of longitudinal fields," Appl. Phys. Lett. **82**, 4596–4598 (2003).
26. K. Kitamura, K. Sakai, and S. Noda, "Sub-wavelength focal spot with long depth of focus generated by radially polarized, narrow-width annular beam," Opt. Express **18**, 4518–4525 (2010).
27. B. Jia, X. Gan, and M. Gu, "Direct observation of a pure focused evanescent field of a high numerical aperture objective lens by scanning near-field optical microscopy," Appl. Phys. Lett. **86**, 131110 (2005).
28. J. Wang, Q. Wang, and M. Zhang, "Development and prospect of near-field optical measurements and characterizations," Front. Optoelectron. **5**, 171–181 (2012).
29. S. N. Khonina, S. V. Karpeev, S. V. Alferov, D. A. Savelyev, J. Laukkanen, and J. Turunen, "Experimental demonstration of the generation of the longitudinal e-field component on the optical axis with high-numerical-aperture binary axicons illuminated by linearly and circularly polarized beams," J. Opt. **15**, 085704 (2013).
30. S. V. Alferov, S. N. Khonina, and S. V. Karpeev, "Study of polarization properties of fiber-optics probes with use of a binary phase plate," J. Opt. Soc. Am. A **31**, 802–807 (2014).
31. V. V. Kotlyar, S. S. Stafeev, Y. Liu, L. O'Faolain, and A. A. Kovalev, "Analysis of the shape of a subwavelength focal spot for the linearly polarized light," Appl. Opt. **52**, 330–339 (2013).
32. W. Chen and Q. Zhan, "Realization of an evanescent Bessel beam via surface plasmon interference excited by a radially polarized beam," Opt. Lett. **34**, 722–724 (2009).
33. S. N. Khonina, S. V. Alferov, and S. V. Karpeev, "Strengthening the longitudinal component of the sharply focused electric field by means of higher-order laser beams," Opt. Lett. **38**, 3223–3226 (2013).
34. A. Carnicer, I. Juvells, D. Maluenda, R. Martínez-Herrero, and P. M. Mejas, "On the longitudinal component of paraxial fields," Eur. J. Phys. **33**, 1235–1247 (2012).
35. F. Maucher, S. Skupin, S. A. Gardiner, and I. G. Hughes, "Creating complex optical longitudinal polarization structures," Phys. Rev. Lett. **120**, 163903 (2018).
36. S. N. Khonina, A. V. Ustinov, and A. P. Porfirev, "Vector Lissajous laser beams," Opt. Lett. **45**, 4112–4115 (2020).
37. L. Zundel, J. R. Deop-Ruano, R. Martínez-Herrero, and A. Manjavacas, "Lattice resonances excited by finite-width light beams," ACS Omega **7**, 31431–31441 (2022).

38. M. Gell-Mann, "Symmetries of baryons and mesons," Phys. Rev. **125**, 1067–1084 (1962).
39. T. Setälä, A. Shevchenko, M. Kaivola, and A. T. Friberg, "Degree of polarization for optical near fields," Phys. Rev. E **66**, 016615 (2002).
40. C. J. R. Sheppard, "Jones and Stokes parameters for polarization in three dimensions," Phys. Rev. A **90**, 023809 (2014).
41. M. Born and E. Wolf, *Principles of Optics: Electromagnetic Theory of Propagation, Interference and Diffraction of Light*, 7th ed. (Cambridge University, 1999).
42. B. Richards and E. Wolf, "Electromagnetic diffraction in optical systems. II. Structure of the image field in an aplanatic system," Proc. R. Soc. London A **253**, 358–379 (1959).
43. D. Maluenda, M. Aviñoá, K. Ahmadi, R. Martínez-Herrero, and A. Carnicer, "Experimental estimation of the longitudinal component of a highly focused electromagnetic field," Sci. Rep. **11**, 17992 (2021).
44. R. Martínez-Herrero, A. Carnicer, I. Juvells, and A. S. Sanz, "Uncertainty principle for axial power content of highly focused fields," Opt. Express **28**, 29676–29690 (2020).
45. M. A. Nielsen and I. L. Chuang, *Quantum Computation and Quantum Information* (Cambridge University, 2000).
46. M. Nieto-Vesperinas and X. Xu, "The complex Maxwell stress tensor theorem: the imaginary stress tensor and the reactive strength of orbital momentum. A novel scenery underlying electromagnetic optical forces," Light Sci. Appl. **11**, 297 (2022).
47. V. Arrizón, "Complex modulation with a twisted-nematic liquid-crystal spatial light modulator: double-pixel approach," Opt. Lett. **28**, 1359–1361 (2003).
48. B. Hao and J. Leger, "Experimental measurement of longitudinal component in the vicinity of focused radially polarized beam," Opt. Express **15**, 3550–3556 (2007).
49. J. R. Fienup, "Reconstruction of an object from the modulus of its Fourier transform," Opt. Lett. **3**, 27–29 (1978).